Draft version March 7, 2022
Typeset using LaTeX **twocolumn** style in AASTeX63

arXiv:2105.02734v2 [astro-ph.HE] 22 Jun 2021

Pursuing the origin of the gamma rays in RX J1713.7−3946 quantifying the hadronic and leptonic components

Yasuo Fukui [1], Hidetoshi Sano [1,2], Yumiko Yamane [1], Takahiro Hayakawa [1], Tsuyoshi Inoue [1], Kengo Tachihara [1], Gavin Rowell [3] and Sabrina Einecke [3]

[1] *Department of Physics, Nagoya University, Furo-cho, Chikusa-ku, Nagoya 464-8601, Japan; fukui@a.phys.nagoya-u.ac.jp*
[2] *Division of Science, National Astronomical Observatory of Japan, Mitaka, Tokyo 181-8588, Japan; hidetoshi.sano@nao.ac.jp*
[3] *School of Physical Sciences, The University of Adelaide, North Terrace, Adelaide, SA 5005, Australia*

ABSTRACT

We analyzed the TeV gamma-ray image of a supernova remnant RX J1713.7−3946 (RX J1713) through a comparison with the interstellar medium (ISM) and the non-thermal X-rays. The gamma-ray datasets at two energy bands of >2 TeV and >250–300 GeV were obtained with H.E.S.S. (H. E. S. S. Collaboration 2018; Aharonian et al. 2007) and utilized in the analysis. We employed a new methodology which assumes that the gamma-ray counts are expressed by a linear combination of two terms; one is proportional to the ISM column density and the other proportional to the X-ray count. We then assume these represent the hadronic and leptonic components, respectively. By fitting the expression to the data pixels, we find that the gamma-ray counts are well represented by a flat plane in a 3D space of the gamma-ray counts, the ISM column density and the X-ray counts. The results using the latest H.E.S.S. data at $4'.8$ resolution show that the hadronic and leptonic components occupy $(67 \pm 8)\%$ and $(33 \pm 8)\%$ of the total gamma rays, respectively, where the two components have been quantified for the first time. The hadronic component is greater than the leptonic component, which reflects the massive ISM of $\sim 10^4$ $M_\odot$ associated with the SNR, lending support for the acceleration of the cosmic-ray protons. There is a marginal hint that the gamma rays are suppressed at high gamma-ray counts which may be ascribed to the second order effects including the shock-cloud interaction and the penetration-depth effect.

Keywords: cosmic rays — gamma rays: ISM — ISM: clouds — ISM: supernova remnants — ISM: individual objects (RX J1713.7−3946)

1. INTRODUCTION

RX J1713.7−3946 (hereafter referred to as RX J1713) is the brightest TeV gamma-ray and non-thermal X-ray supernova remnant (SNR) as revealed by the H.E.S.S. telescope array (Aharonian et al. 2004, 2006) and *ROSAT* X-ray observations (Pfeffermann & Aschenbach 1996), and has been the primary target where the gamma-ray origin can be established. The gamma-rays are produced either by the leptonic origin or the hadronic origin in a SNR. In the leptonic process cosmic-ray (CR) electrons energize the low-energy photons into the gamma-rays, and in the hadronic process CR protons react with the interstellar protons to produce neutral pions which decay into two gamma-rays. If the hadronic process is established, it provides evidence for CR acceleration in a SNR. Considerable effort has been made in modeling the broad band radiation spectrum in the SNR (e.g., Aharonian et al. 2006; H. E. S. S. Collaboration 2018, see also the references therein), and it is shown that either of the two mechanisms can reproduce the observed spectrum. It still remains unsettled what is the dominant gamma-ray production mechanism in RX J1713. It is also shown that leptonic Bremsstrahlung is not effective (e.g., Zirakashvili & Aharonian 2010, hereafter ZA10) and is not considered in the present work.

ZA10 (see also references therein) developed detailed theoretical modelling of the high and very high energy (HE and VHE) radiation of the SNR and presented models of the radiation spectrum in the diffusive shock acceleration (DSA) scheme of CRs (e.g., Bell 1978; Blandford & Ostriker 1978). These authors discussed the leptonic and hadronic origins of the gamma-ray production as well as a composite origin by referring to the CO dense cores overtaken by the SNR shock (Fukui et al. 2003, F03 hereafter; Fukui 2008), where the CO emission is used as proxy for H_2. Other theoretical studies (e.g., Ellison et al. 2010) argued for the leptonic process, be-

cause the gas density, if assumed to be uniform, required to produce gamma rays via the hadronic process will produce significant thermal X-rays, which contradicts the observed purely non-thermal X-rays (Koyama et al. 1997; Tanaka et al. 2008; for thermal X-rays observed in a local spot, (see also Katsuda et al. 2015). The non-thermal X-rays show spatial distribution similar to the gamma rays, which may suggest the leptonic component (e.g., Aharonian et al. 2006; H. E. S. S. Collaboration 2018).

F03 identified the CO gas at $\sim -10\,\mathrm{km\,s^{-1}}$ interacting with RX J1713 by observations with the NANTEN telescope, and determined a kinematical distance of the SNR to be 1 kpc (see the appendix A for more detail). This value is consistent with the latest estimation of 1.12 ± 0.01 kpc (Leike et al. 2021). F03 further found that a CO cloud named peak D, having a size of $\sim 5' \times 10'$ (see Figure 2 of F03), shows a good coincidence with the TeV gamma ray peak, and suggested that the peak D cloud plays a role of target protons in the hadronic gamma-ray production. Subsequently, Moriguchi et al. (2005) and Sano et al. (2013) extended a list of CO peaks in RX J1713 based on the NANTEN observations. Aharonian et al. (2006) compared the NANTEN CO distribution with the H.E.S.S. TeV gamma-ray image and examined both leptonic and hadronic scenarios as the origin of the gamma rays. These authors found that TeV gamma rays show a similar trend to the CO distribution while their correspondence is not good especially in the south- eastern rim of the TeV gamma-ray shell. Fukui et al. (2012, F12 hereafter) thought that not only H_2 but also H I is important as target protons for the hadronic process. These authors showed that the total interstellar medium (ISM) in RX J1713 consists of both atomic and molecular protons, and demonstrated that the ISM shows a good spatial correspondence with the TeV gamma rays observed with H.E.S.S. F12 interpreted this as support for the hadronic origin, while the effective spatial resolution employed ∼4 pc, was not sufficiently high to resolve the degeneracy between the gamma-ray and X-ray distributions, leaving room for leptonic gamma rays.

The Fermi collaboration (Abdo et al. 2011) revealed a hard gamma-ray spectrum in RX J1713 and argued for the leptonic gamma-rays by assuming uniform ISM distribution. Inoue et al. (2012, IYIF12 hereafter) carried out magneto-hydrodynamics (MHD) simulations of the shock-cloud interaction in the realistic clumpy ISM distribution and showed that the interaction makes the magnetic field highly turbulent with field strength up to ∼1 mG around dense cores. Furthermore, IYIF12 derived an expression of the penetration depth of CRs into dense cores and argued that the energy-dependent penetration depth hardens the hadronic gamma-ray spectrum toward the dense cores into one similar to the spectrum observed with Fermi. Prior to IYIF12, the effect of the penetration depth in dense cores was pointed out in terms of the CR diffusion coefficient by Gabici et al. (2007), while hydrodynamical simulations of the shock interaction were not undertaken. ZA10 also suggested hardening of the gamma-ray spectrum in the clumpy ISM qualitatively, and Gabici & Aharonian (2014) demonstrated the hard gamma-ray spectrum in clumpy ISM by considering the CR penetration limited by the diffusion coefficient. Most recently, the new H.E.S.S. gamma-ray data were released, where the sensitivity was improved by a factor of two at three-time better spatial resolution (H. E. S. S. Collaboration 2018) than the previous H.E.S.S. data (Aharonian et al. 2006). The new spatial resolution 1.4 pc at > 2 TeV is still not good enough to fully resolve the gamma-ray/X-ray degeneracy, and the debate on the two origins is ongoing.

It is generally expected that the observed gamma rays are combination of the leptonic and hadronic gamma rays, where the former is proportional to the CR electrons and the low-energy photons and the latter to the CR protons and the ISM protons (e.g., Aharonian et al. 1994; Drury et al. 1994; Zirakashvili & Aharonian 2010). The CR electrons are to a first approximation proportional to the non-thermal X-rays for the inverse Compton scattering in the uniform background photon field (e.g., the Cosmic Microwave Background), while the shock-cloud interactions may vary the relationship through the amplification of the magnetic field, especially around the dense cores (IYIF12). Such amplification became clear through enhanced X-rays as revealed observationally by Sano et al. (2010, 2013). Furthermore, the penetration depth of CRs may become limited toward dense cores, leading to suppress the hadronic gamma-rays (Gabici et al. 2007). The effect of the penetration depth has not been directly shown observationally except for the GeV gamma-ray spectrum by Fermi LAT (e.g., IYIF12), while spatial anti-correlation between dense cores and gamma rays may become apparent if angular resolution becomes sufficiently high. It is in particular an important challenge to discern the two gamma-ray origins, and the new H.E.S.S. data may offer an opportunity for such an attempt.

The aim of the present paper is to revisit the comparison between the ISM and the gamma rays by using the new H.E.S.S. gamma-ray data in order to pursue the spatial correspondence revealed by F12. This paper is organized as follows. Section 2 describes the datasets used in the work. Section 3 presents the results of the

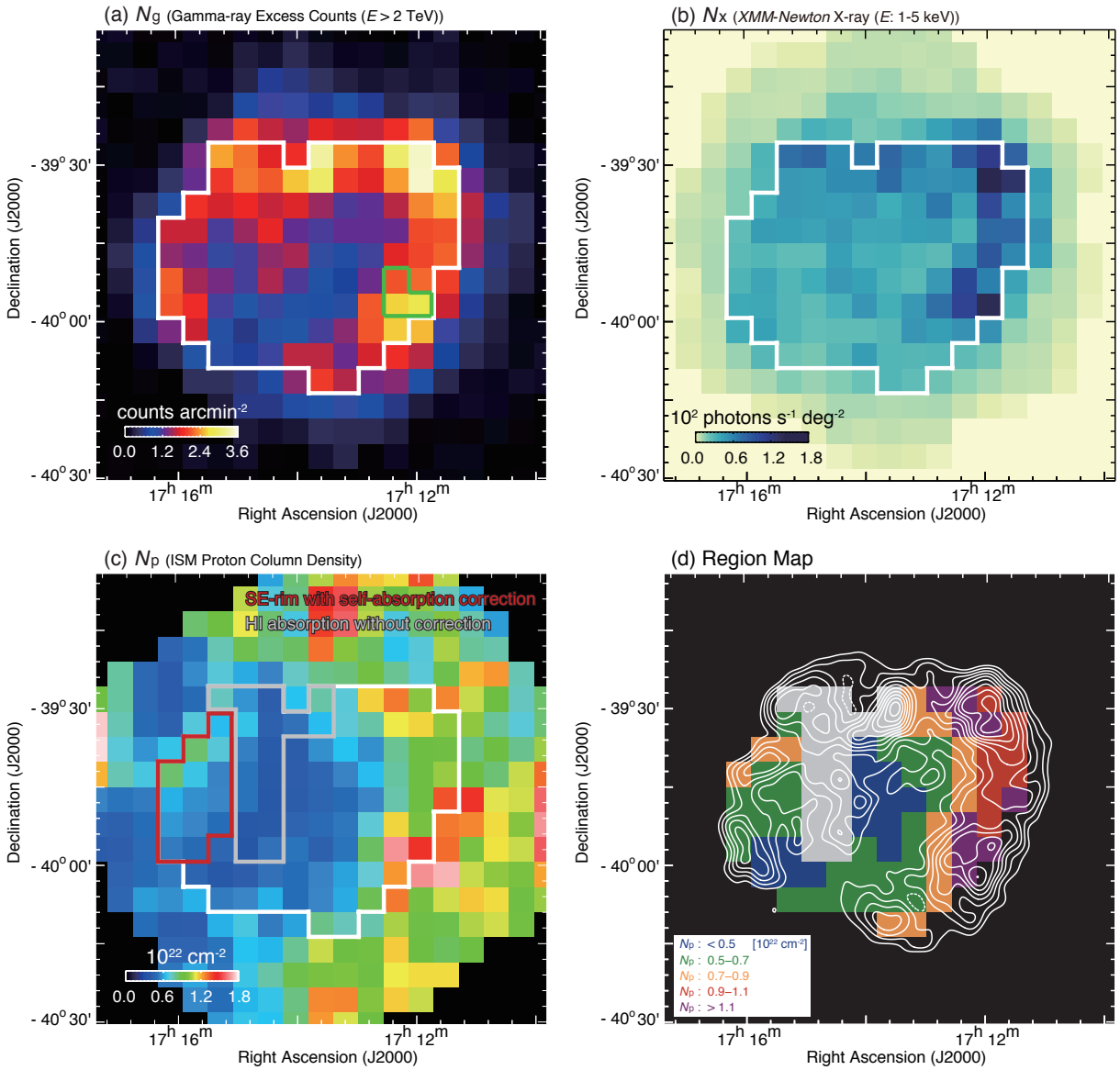


Figure 1. Spatial distributions of (a) $N_{\rm g}$ (H.E.S.S. TeV gamma-rays ($E > 2$ TeV, H. E. S. S. Collaboration 2018), (b) $N_{\rm x}$ (*XMM-Newton* X-rays (E: 1.0–5.0 keV)), and (c) $N_{\rm p}$ (ISM proton column density, F12). Three pixels within the green lines are discussed in Section 4.2. White polygon indicates region to be used for the present analysis. Red polygon indicates region where we make correction for the H I absorption (see Section 2.3). The pixels within the gray polygon represents region where there is no reliable way to assume background H I without self-absorption and are excluded in the present analysis (see text). (d) Gray pixels are the same as region within the gray polygon. Blue, green, orange, red, and purple pixels represent the regions where $N_{\rm p}$ less than 0.5, 0.5–0.7, 0.7–0.9, 0.9–1.1, more than $1.1 \times 10^{22}\,{\rm cm}^{-2}$, respectively. Superposed white contours indicate TeV gamma-rays excess counts. The lowest contour level and contour intervals are 12 and 3 excess counts, respectively.

comparison among the gamma-rays, ISM, and X-rays. In Section 4, discussion on the comparison is presented and the origin of the gamma rays is explored into detail. Section 5 gives conclusions.

2. OBSERVATIONAL DATA

In Figures 1, we show the spatial distributions of the three datasets rebinned to the resolution of the H.E.S.S. data 1.4 pc. They include the H.E.S.S. >2 TeV energy band, the *XMM-Newton* X-rays, and the ISM, in Figures 1(a), 1(b), and 1(c), respectively, and Figure 1(d) shows the areas which indicate regions of different ISM column density. We explain their details in the following.

2.1. *X-Ray Data*

We used archival datasets obtained with *XMM-Newton* to create images of synchrotron X-rays in RX J1713.7−3946. We utilized the *XMM-Newton* Sci-

Table 1. Summary of *XMM-Newton* archive data in RX J1713.7−3946

					Exposure		
Observation ID	α_{J2000} (degree)	δ_{J2000} (degree)	Start Date (yyyy-mm-dd hh:mm:ss)	End Date (yyyy-mm-dd hh:mm:ss)	MOS1 (ks)	MOS2 (ks)	pn (ks)
0093670101	258.55	−39.43	2001-09-05 03:42:27	2001-09-05 06:29:06	1.7	1.7	9.9
0093670201	258.00	−39.52	2001-09-05 08:35:57	2001-09-05 11:22:35	10.9	7.9	2.8
0093670301	257.97	−39.93	2001-09-08 01:09:54	2001-09-08 04:17:28	14.8	15.1	10.9
0093670401	258.87	−40.02	2002-03-14 15:59:04	2002-03-14 19:37:57	11.4	11.7	6.3
0093670501	258.37	−39.83	2001-03-02 19:04:04	2001-03-02 21:37:24	12.6	12.7	7.5
0203470401	258.55	−39.43	2004-03-25 08:54:49	2004-03-25 12:36:08	15.6	15.9	10.3
0203470501	258.00	−39.53	2004-03-25 14:28:10	2004-03-25 18:09:30	13.7	13.7	10.9
0207300201	258.37	−39.83	2004-02-22 14:16:34	2004-02-22 23:42:50	13.1	13.7	—
0502080101	258.84	−39.66	2007-09-15 05:12:23	2007-09-15 13:15:04	5.9	6.9	7.1
0551030101	258.38	−40.20	2008-09-27 17:46:20	2008-09-27 23:31:58	23.6	23.8	19.6
0740830201	258.37	−39.83	2014-03-02 07:43:38	2014-03-03 15:29:29	88.8	92.1	—
0743030101	258.93	−40.05	2015-03-10 22:17:03	2015-03-11 20:47:16	66.3	67.2	54.1
0804300101	257.91	−39.53	2018-08-26 03:43:25	2018-08-27 03:17:50	82.7	83.0	68.3
0804300301	258.00	−40.17	2018-03-29 17:54:06	2018-03-30 14:55:31	62.5	64.2	45.7
0804300401	258.44	−40.19	2018-03-31 02:35:50	2018-04-01 00:06:36	65.8	72.6	38.2
0804300501	258.35	−39.49	2018-03-25 04:46:15	2018-03-26 15:12:56	103.8	108.0	84.2
0804300601	258.99	−39.70	2018-03-19 18:04:00	2018-03-20 15:40:49	60.3	62.3	53.7
0804300701	258.80	−39.41	2018-03-21 05:02:06	2018-03-22 03:24:32	76.0	81.1	60.1
0804300801	258.69	−39.77	2017-08-30 17:50:43	2017-08-31 05:39:09	44.6	44.6	38.8
0804300901	258.34	−39.26	2017-08-29 16:29:26	2017-08-30 04:04:54	27.8	28.6	19.7
0804301001	257.92	−39.90	2018-03-23 16:39:29	2018-03-24 15:18:32	20.8	67.7	48.8

NOTE—All exposure times represent the flare-filtered exposure.

ence Analysis System (SAS; Gabriel et al. 2004) version 18.0.0 and HEAsoft version 6.27.1 to analyze both the EPIC-pn and EPIC-MOS datasets with a total of 21 pointings (see Table 1). We reprocessed all the Observation Data Files (ODF) following standard procedures provided as the *XMM-Newton* extended source analysis software (ESAS; Kuntz & Snowden 2008). The good time intervals (GTI) after filtering soft proton flares are shown in Table 1. To generate quiescent particle background (QPB) images and exposure maps for each observation, we run procedures of "mos-/pn-back" and "mos-/pn-filter." The procedure "merge_comp_xmm" was used to combine the 21-pointing data. Note that we excluded 1) CCDs chips affected by strong stray light especially for high-energy bands and 2) short GTI data less than 1 ks to improve the imaging quality. Finally, we applied an adaptive smoothing using the procedure "adapt_merge", where the pixel sizes and smoothing counts were set to 6″ and 80 counts, respectively. We generated QPB-subtracted, exposure-corrected, and adaptively smoothed images in the energy bands of 0.5–0.8, 0.8–1.0, 1.0–2.0, 2.0–3.0, 3.0–5.0, and 1.0–5.0 keV[1]. Because the X-ray image in the energy band of 1.0–5.0 keV is not subject to significant absorption by the ISM (see Figures 8 and 9 in Appendix B), we used the 1.0–5.0 keV image for the comparative analysis. In the present analyses, we flagged two bright point sources, 1WGA J1714.4−3945 and 1WGA J1713.4−394, considering their point spread functions using the procedure

[1] Although the astrophysical X-ray background such as the Galactic diffuse X-ray emission is associated with the QPB-subtracted image, the background level is significantly lower than the synchrotron radiation from RX J1713.7−3946 (e.g., H. E. S. S. Collaboration 2018). It means that the small scale structures (or spatial variations of X-rays) of the SNR are not affected by the X-ray background. In the present paper, we did not subtract such X-ray background from the QPB-subtracted images.

"cheese" implemented in ESAS. We then rebinned the data to match grid size 4.′8 of the H.E.S.S. gamma-ray data. Here we averaged data values of X-rays within each pixel area, except for the point-sources flagged-areas. The rebinned X-ray image is presented as Figure 1(b). The X-ray count $N_{\rm x}$ is given in unit of 10^2 photons s^{-1} degree^{-2} and is used throughout the present paper.

2.2. *H.E.S.S. TeV Gamma-Ray Data*

The gamma-ray data consist of two energy ranges, above 250 GeV (broad energy band) and above 2 TeV (high energy band), which are the combined data taken in several sessions over 2004, 2005, 2011, and 2012 (H. E. S. S. Collaboration 2018). The angular resolution (full-width half maximum; FWHM) is 6.′6 for the broad energy band and 4.′8 for the high energy band, corresponding to the spatial resolution of 1.9 pc and 1.4 pc, respectively, at a distance of 1 kpc. We also used the previous H.E.S.S. data in Aharonian et al. (2007).The energy band is >300 GeV, similar to the broad energy band of H. E. S. S. Collaboration (2018), and the resolution is 8.′4 corresponding to 2.5 pc.

The >2 TeV dataset is named H.E.S.S.18($E > 2$ TeV), which provides the highest resolution and largest number of pixels among the H.E.S.S. data available. The >250 GeV dataset is named H.E.S.S.18($E > 250$ GeV) and the previous H.E.S.S data is named H.E.S.S.07. In addition to H.E.S.S.18($E > 2$ TeV) at 4.′8 resolution, for testing dependence on angular resolution and gamma-ray energy, we analyze five H.E.S.S. datasets with lower resolution as listed in Table 2; two of them are H.E.S.S.18($E > 2$ TeV) smoothed to 6.′6 resolution and H.E.S.S.18($E > 250$ GeV) having 6.′6 resolution (H. E. S. S. Collaboration 2018), and three of them are H.E.S.S.18($E > 2$ TeV) smoothed to 8.′4 resolution, H.E.S.S.18($E > 250$ GeV) smoothed to 8.′4 resolution, and H.E.S.S.07 having 8.′4 resolution. In the following analyses, all the X-ray data and the ISM data are binned to the same pixel size with the H.E.S.S. data. The gamma ray count $N_{\rm g}$ is given in unit of excess counts arcmin^{-2} throughout this paper. The error was estimated as the square-root of the total excess counts within each pixel in conjunction with correction for the oversampling effect.

The gamma-ray shell is peaked at ∼6 pc in radius, beyond which the gamma rays show sharp decline. This suggests that CR or electron energy density decreases beyond the peak (H. E. S. S. Collaboration 2018; F12). We assume that the CR energy density is nearly uniform within the shell and restrict the area of the analysis to the interior within the gamma-ray peak. By this restriction we eliminate the outer region where CR energy density decreases as shown by the white solid lines in Figure 1(a).

2.3. *ISM Proton Distribution*

We follow F12 in calculating the ISM column density, which includes both molecular and atomic hydrogen. The molecular column density $N(\rm H_2)$ is calculated from the integrated intensity of the ^{12}CO($J = 1$–0) emission W(CO) (K km s^{-1}) for an $X_{\rm CO}$ factor 2×10^{20} cm^{-2} (K km s^{-1})$^{-1}$ (Bertsch et al. 1993) which is typically found in the Galaxy;

$$N_{\rm p}({\rm H_2})\ ({\rm cm^{-2}}) = 2 \times N({\rm H_2}) = 4 \times 10^{20}\ W({\rm CO})\ ({\rm K\,km\,s^{-1}}). \quad (1)$$

The atomic hydrogen column density N(H I) (cm^{-2}) was calculated from the integrated intensity W(H I) (K km s^{-1}) of the 21 cm H I emission by adopting the optically thin approximation as follows;

$$N({\rm H\ I})\ ({\rm cm^{-2}}) = 1.832 \times 10^{18}\ W({\rm H\ I})\ ({\rm K\,km\,s^{-1}}). \quad (2)$$

In the present paper, we used the velocity integration range of W(CO) or W(H I) from −20 to 0 km s^{-1}, which is compatible with the previous study (F12).

Figure 1(c)shows the ISM column density distribution in units of 10^{22} cm^{-2}. We averaged values of column density within each pixel area, as with the X-ray datasets. We also make correction for the H I self-absorption in the SE cold H I cloud by using the method in Sato & Fukui (1978), where the background H I emission is assumed by a straight line as explained in F12. Some of the other positions may be subject to self-absorption. Figure 2 shows two cuts of H I profiles toward the region including H I with self-absorption, and indicates that a few spectra have clear dips and that some have flat spectra have clear dips in addition to some having flat spectra, e.g., E and F in cut1 and cut2. It is possible that the flat spectra are due to self-absorption, whereas there is no reliable way to assume background H I without self-absorption. If we assume a background H I emission, identical to that at position H in cut2, we estimate W(H I) becomes larger than the optically thin case by a factor of 2, while the correction is arbitrary. We therefore selected 18 pixels by eye inspection as those with uncertain background emission as enclosed by the gray solid lines in Figure 1(c), and excluded them in the present analysis in order not to impair the accuracy. It is possible that the H I emission is affected by the optically thick H I (Fukui et al. 2014, 2015, 2018), whereas the direction of RX J1713 is in the Galactic plane, not allowing to make a direct

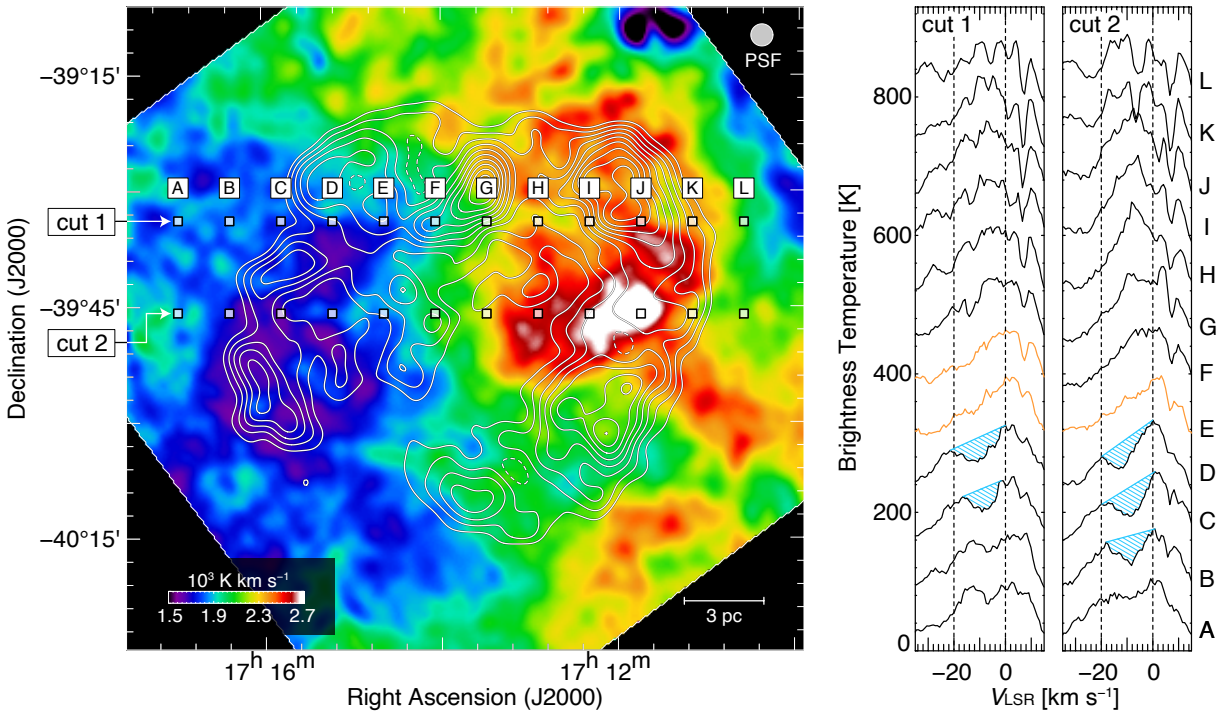


Figure 2. Integrated intensity map of H I overlaid with TeV gamma-ray contours (*left panel*), and H I profiles (*middle and right panels*). The contour levels are the same as in Figure 1(d). The integration velocity range of H I is from −20.6 to −0.8 km s^{-1}. The H I profiles are shown in along cuts 1 and 2. Each profile position (A–L) indicates square symbols labeled A–L in the left panel. The-self absorption dips are shown by the blue hatch with the straight background H I, and the yellow profiles show the flat ones without correction for self absorption.

estimate of the H I optical depth by using the Planck dust emission (Planck Collaboration 2014). We therefore did not attempt to apply further the H I optical depth correction.

The total hydrogen column density is calculated as follows;

$$N_{\rm p} = N_{\rm p}({\rm H_2 + H\,I}) = 2 \times N_{\rm p}({\rm H_2}) \; + \; N({\rm H\,I}). \qquad (3)$$

Considering these ISM proton properties, we denoted the two regions as shown in Figure 1(c); the region where self-absorption is corrected for (14 pixels shown by the red solid lines) is included in the analysis, and that where correction for self-absorption is difficult due to a flat line shape, 18 pixels shown by the gray solid lines, are masked in the analysis. According to F12, the errors in the region with self-absorption are estimated to be <20%, while the errors elsewhere are mostly statistical ones and negligibly small. In Figure 1(d) we divide the pixels into five zones of $N_{\rm p}$, which are used in Section 3. The total number of the pixels after this masking is 75 in H.E.S.S.18 ($E > 2$ TeV). A similar masking was also applied to H.E.S.S.07 and the total number of the pixels is 32.

Details of the respective ISM observations are summarized below.

2.3.1. *The NANTEN CO Data*

We utilize the ^{12}CO(J = 1–0) data at 115.271202 GHz obtained with the NANTEN 4-m millimeter telescope, which were published by Moriguchi et al. (2005). The observations were carried out by using the position-switching method with a grid spacing of 2.′0. The mapped area is ∼1.9 degree^2 in the region of 346.°7–348.°0 in Galactic longitude and of −1.°2–0.°2 in Galactic latitude, including CO peaks A, C, D and L (F03; Moriguchi et al. 2005; Sano et al. 2013). The 4 K cooled Nb superconductor-insulator-superconductor (SIS) mixer was used as the frontend (Ogawa et al. 1990). The typical system temperature was ∼250 K in the single-sideband (SSB), including the atmosphere toward the zenith. The backend was an acousto-optical spectrometer (AOS) with 2048 channels and 250 MHz bandwidth. The CO data cover a velocity range of 600 km s^{-1} with a velocity resolution of 0.65 km s^{-1}. The final data have a beam size of 156 arcsec and typical noise fluctuations of 0.2–0.3 K ch^{-1} (more detailed information, see Section 2 of Moriguchi et al. 2005).

2.3.2. *The ATCA plus Parkes H I Data*

The H I data at 1.4 GHz are from the Southern Galactic Plane Survey (McClure-Griffiths et al. 2005), which

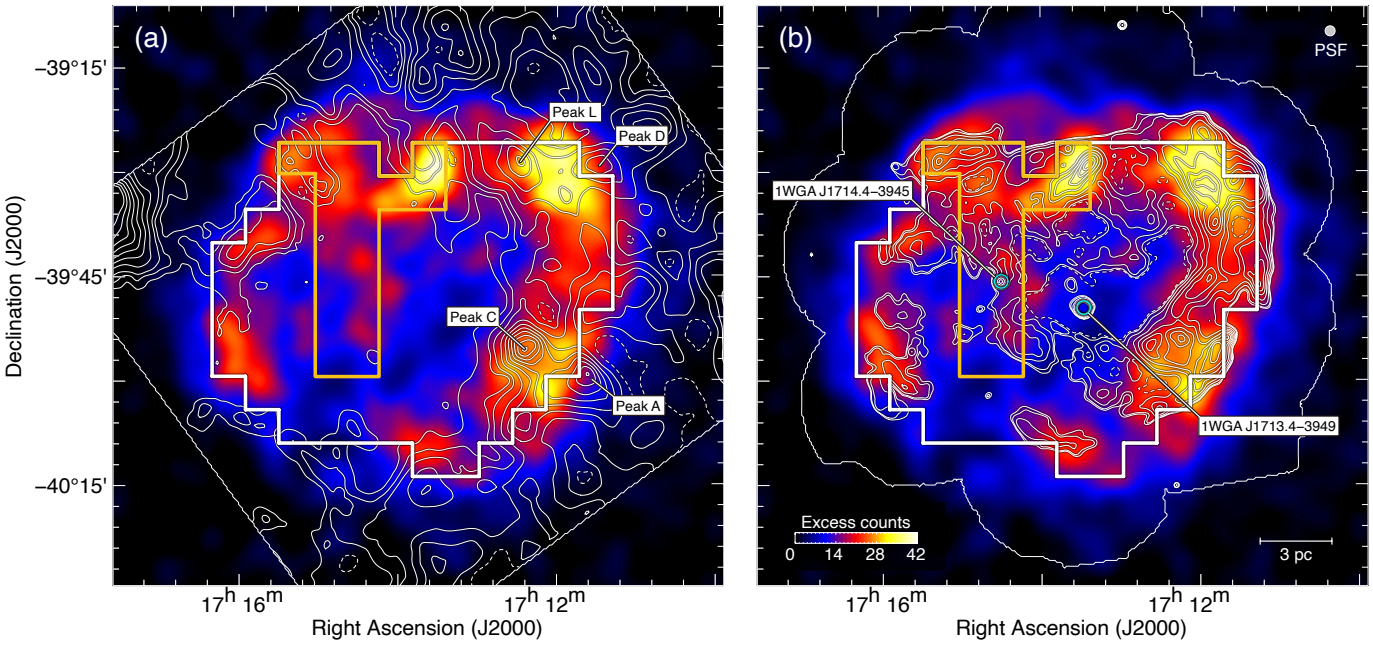


Figure 3. Maps of TeV gamma-rays ($E > 2$ TeV) toward RX J1713.7−3946 overlaid with (a) total proton column density $N_{\rm p}$(H$_2$+H I) (F12) and (b) *XMM-Newton* X-rays (E: 1.0–5.0 keV). The contour levels are 6, 7, 8, 10, 12, 14, 16, 18, 20, and 22×10^{21} cm^{-2} for $N_{\rm p}$(H$_2$+H I); and 37, 40, 49, 64, 85, 112, 145, and 184 photons s^{-1} degree^2 for X-rays. The white polygon is the same as shown in Figure 1. The orange polygon is the same as gray polygon in Figure 1(c). Thin rectangle and curve indicate observed regions of $N_{\rm p}$(H$_2$+H I) and X-rays, respectively. The positions of CO peaks A, C, D, and L are shown. The two prominent X-ray point sources, 1WGA J1714.4−3945 and 1WGA J1713.4−3949, are also shown in circles.

were obtained by combining the H I datasets with the Australia Telescope Compact Array (ATCA) and the Parkes Radio Telescope. The beam size 2.′2 is high enough to spatially resolve the cool H I cloud in the southeast-rim with a self-absorption profile. The typical noise fluctuations are 1.9 K at a velocity resolution of 0.82 km s^{-1}.

3. CORRELATION AMONG THE GAMMA RAYS, THE ISM AND THE X-RAYS

Figures 3(a) and 3(b) show gamma-ray distribution superposed on the ISM contours and X-ray contours, respectively, which suggest that the three distributions are fairly similar to each other. This is consistent with the hybrid picture of the two gamma-ray origins (Section 1). In the following, we describe the analyses of H.E.S.S.18($E > 2$ TeV) in Sections 3.1 and 3.2, and those of H.E.S.S.18($E > 250$ GeV) and H.E.S.S.07, and of the spatially smoothed H.E.S.S.18 data in Section 3.4.

3.1. *A Unified Fitting in the 3D Space of $N_{\rm p}$–$N_{\rm x}$–$N_{\rm g}$*

Motivated by the basic picture above regarding the gamma-ray origin, we formulate the gamma-ray counts as a combination of two terms, one proportional to $N_{\rm p}$ and the other proportional to $N_{\rm x}$ as a first approximation. Simple approximate relationships of $N_{\rm g}$ are given in a line of sight as follows; the hadronic gamma rays $N_{\rm g}$(hadronic) via the p-p reaction is proportional to the CR proton column density $N_{\rm p}$(CR) times the ISM proton column density $N_{\rm p}$(ISM) [$N_{\rm g}$(hadronic) $\propto N_{\rm p}$(CR)$\times N_{\rm p}$], and the leptonic gamma rays via the inverse Compton scattering $N_{\rm g}$(leptonic) is proportional to the CR electron column density $N_{\rm e}$(CR) times the uniform low-energy photon density $N_{\rm photon}$(CMB=the Cosmic Microwave Background) [$N_{\rm g}$(leptonic) $\propto N_{\rm e}$(CR) $\times N_{\rm photon}$(CMB)]. Noting that the nonthermal X-ray count $N_{\rm x}$ is proportional to $N_{\rm e}$(CR) times the squared magnetic field flux density B^2 [$N_{\rm x} \propto N_{\rm e}$(CR) $\times B^2$], $N_{\rm g}$(leptonic) is hence proportional to $N_{\rm x}$ times ($N_{\rm photon}$(CMB) $/B^2$) [$N_{\rm g}$(leptonic) $\propto N_{\rm x}\times$ ($N_{\rm photon}$(CMB)$/B^2$)] (e.g., Aharonian et al. 1997).

As a result, $N_{\rm g}$ for the combination is given as follows;

$$N_{\rm g} = aN_{\rm p} + bN_{\rm x}, \tag{4}$$

where the coefficient a is proportional to $N_{\rm p}$(CR) and coefficient b to $N_{\rm photon}$(CMB)$/B^2$. Here, we can see that the a and b coefficients respectively encapsulate a global dependence on the cosmic ray energy density and the CMB/B-field energy density ratio, as a way to provide estimates of the hadronic and leptonic fractions. We assume here that the magnetic field strength

Table 2. Summary of the multiple linear regression

Dataset							F-test	
Energy band	Pixel size	n	red$r$	a	b	R^2	F	$F_{0.01}(2, n-2)$
(1)	(2)	(3)	(4)	(5)	(6)	(7)	(8)	(9)
H.E.S.S.18								
$E > 2\,\mathrm{TeV}$	4′.8	75	0.71	1.45 ± 0.17	1.02 ± 0.24	0.92	441.1	4.9
	6′.6	36	0.74	1.39 ± 0.24	1.10 ± 0.34	0.97	660.0	5.3
	8′.4	23	0.80	1.37 ± 0.28	1.05 ± 0.41	0.98	646.9	5.8
$E > 250\,\mathrm{GeV}$	6′.6	36	0.74	10.6 ± 1.7	7.9 ± 2.4	0.97	641.3	5.3
	8′.4	23	0.80	10.4 ± 1.8	8.1 ± 2.6	0.99	896.1	5.8
H.E.S.S.07								
$E \gtrsim 300\,\mathrm{GeV}$[a]	8′.4	23	0.80	1.87 ± 0.27	1.07 ± 0.40	0.97	383.0	5.8

[a] We presumed the same energy threshold that was used for the spectral analysis in Aharonian et al. (2007).

NOTE— Columns (1) – (3): energy band, pixel size and number of pixels of the dataset, (see Section 2.2), red(4) correlation coefficient between N_p and N_x, (5) and (6): regression coefficients estimated by Equation (C4) and standard deviations of them (the square root of the diagonal elements of Equation (C5)). (7): coefficient of determination given by Equation (C6), (8): F-statistic given by Equation (C7) and (9) critical F-value with $(2, n-2)$ degrees of freedom for 1% significance level. See Appendix C for further details.

B is uniform in most of the volume as suggested by IYIF12. We consider that the CMB photon density is also uniform and that additional stellar photons are insignificant (e.g., Tanaka et al. 2008). In addition, the energy density of CRs is assumed to be uniform within the SNR shell which is consistent with the model calculations (e.g., ZA10).

We apply Equation (4) to the data pixels in a 3D space of N_p-N_x-N_g. For this purpose, we developed the formulation for the least-squares fitting as given in Appendix C.1 in the present work and applied it to H.E.S.S.18($E > 2\,\mathrm{TeV}$). As a result, we obtained a multiple linear regression plane given by the following relation;

$$\hat{N_\mathrm{g}} = (1.45 \pm 0.17) \times N_\mathrm{p} + (1.02 \pm 0.24) \times N_\mathrm{x}, \quad (5)$$

for all the 75 pixels across the ISM/X-ray/gamma 3D space. The hat symbol (ˆ) put on N_g means that it is predicted by the regression. Table 2 lists a and b, and shows that the fitting is reasonably good with the coefficient of determination $R^2 = 0.92$ (see Appendix C.2), which means that 90% of the variance in N_g is predictable from N_p and N_x. Figure 4 shows the plane with the 75 pixels, and we confirm the good fitting. In Figure 5 we show a plot of $\Delta N_\mathrm{g} = N_\mathrm{g} - \hat{N}_\mathrm{g}$ as a function of $\hat{N}_\mathrm{g}$. This corresponds to a side view of the plane in Figure 4 from the direction of $\hat{N}_\mathrm{g}$ = constant. ΔN_g is nearly zero at $\hat{N}_\mathrm{g}$ below 2.0, showing a good fit of the regression for most of the pixels. There seems to be a hint of slight decrease of ΔN_g at $\hat{N}_\mathrm{g}$ above 2.0, although the number of the pixels in this category is 15. The uncertainty in $\hat{N}_\mathrm{g}$ for i-th pixel ($i = 1 \cdots 75$) is given by

$$\sigma(\hat{N}_{\mathrm{g},\,i}) = \left\{ (N_{\mathrm{p},\,i}\,\sigma_a)^2 + [a\,\sigma(N_{\mathrm{p},\,i})]^2 + (N_{\mathrm{x},\,i}\,\sigma_b)^2 + [b\,\sigma(N_{\mathrm{x},\,i})]^2 \right\}^{1/2}, \quad (6)$$

and that of ΔN_g by

$$\sigma(\Delta N_{\mathrm{g},\,i}) = \left[\sigma(N_{\mathrm{g},\,i})^2 + \sigma(\hat{N}_{\mathrm{g},\,i})^2 \right]^{1/2}. \quad (7)$$

Here, $\sigma(N_\mathrm{g})$, $\sigma(N_\mathrm{p})$ and $\sigma(N_\mathrm{x})$ are the uncertainties in N_g, N_p and N_x, and σ_a and σ_b are the standard errors of the estimated a and b (Equation (C5) in Appendix C.1), respectively. Note that we have estimated $\sigma(N_{\mathrm{p},\,i})$ from the rms noise in $W(\mathrm{H\,I})$ and $W(\mathrm{CO})$, without taking into account uncertainty in the X_CO factor.

3.2. *Separation of the Hadronic and Leptonic Origins*

Equation (5) allows us to make a first estimate of the gamma rays of the hadronic and leptonic origins separately. The hadronic component is given by

$$\hat{N}_\mathrm{g}^\mathrm{hadronic} = a N_\mathrm{p} \quad (8)$$

and its uncertainty is

$$\sigma(\hat{N}_\mathrm{g}^\mathrm{hadronic}) = \left\{ (\sigma_a\,N_\mathrm{p})^2 + [a\,\sigma(N_\mathrm{p})]^2 \right\}^{1/2} \sim \sigma_a\,N_\mathrm{p}, \quad (9)$$

Table 3. Estimate of the hadronic- and leptonic-origin gamma-rays

Dataset				Hadronic component			Leptonic component	
Energy band	Pixel size	$\langle \hat{N}_{\rm g} \rangle$	$\langle N_{\rm p} \rangle$	$\hat{N}_{\rm g}^{\rm hadronic}$	$\hat{N}_{\rm g}^{\rm hadronic}/\langle \hat{N}_{\rm g} \rangle$	$\langle N_{\rm x} \rangle$	$\hat{N}_{\rm g}^{\rm leptonic}$	$\hat{N}_{\rm g}^{\rm leptonic}/\langle \hat{N}_{\rm g} \rangle$
(1)	(2)	(3)	(4)	(5)	(6)	(7)	(8)	(9)
H.E.S.S.18								
$E > 2\,$TeV	4.′8	1.56 ± 0.02	0.72	1.04 ± 0.12	$(67 \pm 8)\%$	0.50	0.51 ± 0.12	$(33 \pm 8)\%$
	6.′6	1.57 ± 0.04	0.73	1.01 ± 0.17	$(65 \pm 11)\%$	0.50	0.55 ± 0.17	$(35 \pm 11)\%$
	8.′4	1.54 ± 0.07	0.74	1.01 ± 0.21	$(66 \pm 14)\%$	0.50	0.53 ± 0.20	$(34 \pm 13)\%$
$E > 250\,$GeV	6.′6	11.7 ± 0.3	0.73	7.7 ± 1.2	$(66 \pm 11)\%$	0.50	4.0 ± 1.2	$(34 \pm 10)\%$
	8.′4	11.7 ± 0.4	0.74	7.6 ± 1.3	$(65 \pm 11)\%$	0.50	4.0 ± 1.3	$(35 \pm 11)\%$
H.E.S.S.07								
$E \gtrsim 300\,$GeV	8.′4	1.92 ± 0.06	0.74	1.38 ± 0.20	$(72 \pm 11)\%$	0.50	0.54 ± 0.20	$(28 \pm 10)\%$

NOTE— Columns (1) and (2): energy band and pixel size of the dataset, (3), (4) and (7): spatial averages of observed $N_{\rm g}$ (counts arcmin^{-2}), $N_{\rm p}$ ($10^{22}\,$cm^{-2}) and $N_{\rm x}$ (10^2 photons s^{-1} degree^{-2}), (5) and (8): predicted values of hadronic- and leptonic-origin gamma-rays (counts arcmin^{-2}), (6) and (9): fraction of the hadronic and leptonic components.

where we ignore the second term because $\sigma(N_{\rm p})/N_{\rm p} = 10^{-2}$ is one-order of magnitude smaller than σ_a/a. The leptonic component and its uncertainty are given in a similar manner,

$$\hat{N}_{\rm g}^{\rm leptonic} = bN_{\rm x} \tag{10}$$

and

$$\sigma(\hat{N}_{\rm g}^{\rm leptonic}) \sim \sigma_b\, N_{\rm x}, \tag{11}$$

respectively. By using the coefficients a and b obtained in Section 3.1 (summarized in Table 2) and the spatially-averaged gamma-ray count $\bar{N}_{\rm g} = \sum_i N_{{\rm g},\,i}/n$, ISM proton column density $\bar{N}_{\rm p} = \sum_i N_{{\rm p},\,i}/n$ and X-ray count $\bar{N}_{\rm x} = \sum_i N_{{\rm x},\,i}/n$ listed in Table 3, it is estimated that the hadronic component occupies $(67 \pm 8)\%$ of the total gamma ray count and the leptonic component $(33 \pm 8)\%$. Further discussion is given in Section 4.1.

We checked the effect of adding back the excluded 18 pixels and found that the fitted values for $a = 1.20 \pm 0.18$ and $b = 1.52 \pm 0.24$ (see Equation 4) suggested hadronic and leptonic fractions of $52 \pm 8\%$ and $48 \pm 8\%$ respectively. The hadronic fraction has decreased compared to our main result, as expected, due to the lack of self-absorption corrected leads to an underestimate of $N_{\rm p}$.

3.3. *Positional dependence of the hadronic gamma-ray fraction*

We have obtained the hadronic and leptonic gamma-ray count in each pixel, and are able to compare [the fraction of the hadronic/leptonic gamma rays in the total gamma rays] and [$N_{\rm p}$ or $N_{\rm x}$] over the SNR. In Figure 6, we present a scatter plot between the hadronic gamma ray fraction and $N_{\rm x}$ in all 75 pixels for different ranges of $N_{\rm p}$ values. The hadronic fraction fitted by the model is expressed from Equation (4) as follows;

$$[\text{Hadronic gamma ray fraction}] = \frac{aN_{\rm p}}{\hat{N}_{\rm g}}, \tag{12}$$

which indicates that the fraction increases with $N_{\rm p}$ and decreases with $N_{\rm x}$. The relationships derived from Equation (12) are plotted by the colored thin solid lines in Figure 6, showing a good correspondence with each pixel. The model includes both the hadronic and leptonic components and Figure 6 naturally shows a mixed trend. We find that a high hadronic fraction more than 70 % is found toward low $N_{\rm x} < 0.6$ but not only toward high $N_{\rm p} > 0.9$. It is also notable that more than half of the pixels with a low hadronic fraction less than 60 % have high $N_{\rm p} > 0.9$. These trends are likely caused by the enhanced X-rays toward dense ISM clumps. Figure 6 indicates that there are hadronic-dominated regions with $> 70\%$, whereas there are no such regions dominated by leptonic emission to the same level. We also recognize these trends in Figures 7(a) and 7(b), which show overlays of the hadronic fraction with the distributions of $N_{\rm p}$ and $N_{\rm x}$, respectively. The two figures are somewhat complicated to grasp simply, whereas we recognize that a high hadronic fraction is often found toward regions of low $N_{\rm x}$ as is consistent with Figure 6; they are in the south-eastern rim and in the east of the western bright X-ray shell. These comparisons will provide observational signatures of the two gamma-ray origins, which will be revealed more into depth at higher resolution in the CTA era.

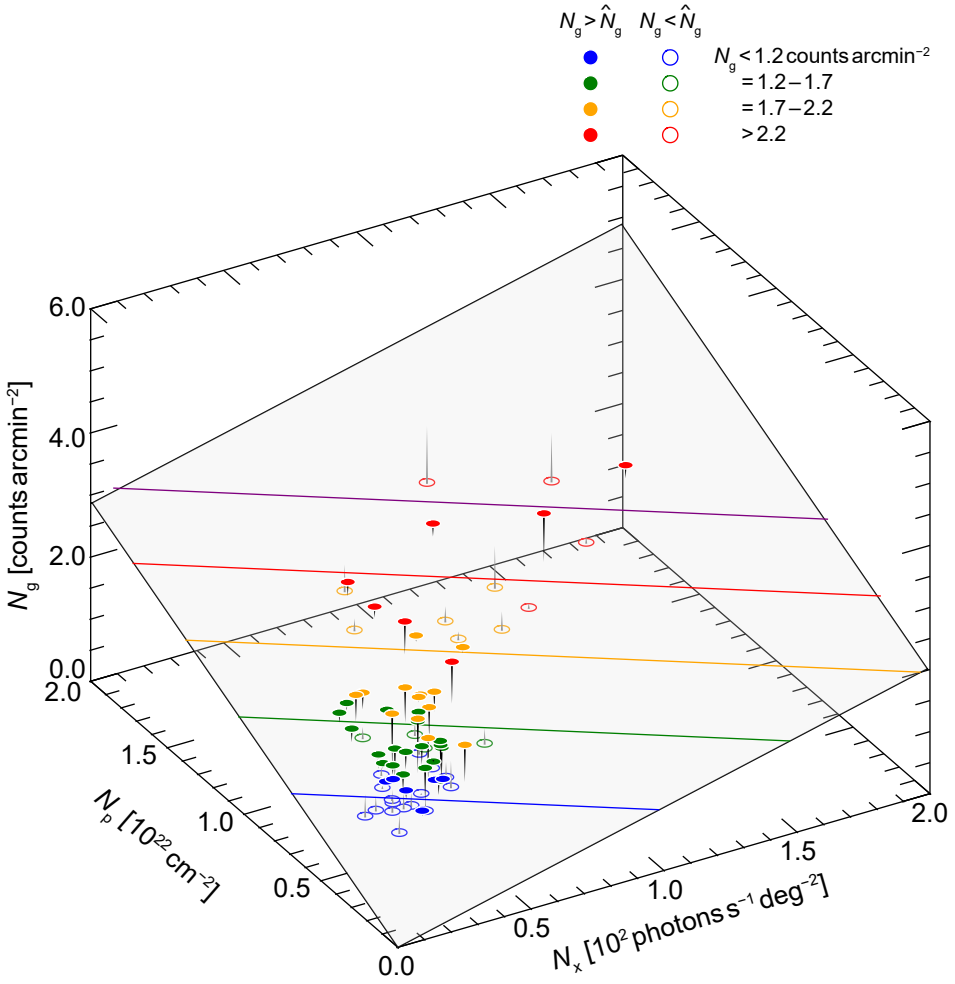


Figure 4. 3D fitting of a flat plane expressed by Equation (5) in the N_p-N_x-N_g space for H.E.S.S.18 ($E > 2$ TeV) with a pixel size of 4′.8. The data pixels are colored by the code in the figure according to N_g, which are shown by the filled and open symbols for those above and below the plane. Each vertical (parallel to the N_g axis) line connects N_g and $\hat{N}_g$. The blue, green, orange, red, and purple lines on the best-fit plane indicate $\hat{N}_g$ = 1.0, 1.5, 2.0, 2.5, and 3.0 counts arcmin^{-2}, respectively.

3.4. *Analyses at lower resolutions*

We made additional analyses of the five H.E.S.S. datasets at resolutions of 6′.6 and 8′.4 as listed in Table 2. The method explained in Sections 3.1 is applied to them and regression flat planes derived are included in Table 2. The planes are used to derive the hadronic and leptonic gamma rays in the same manner explained in Section 3.2.

In Table 3 we find that the hadronic and leptonic gamma rays show similar fractions of (65–72)%:(28–35)% or $\sim 6\sigma$:3σ for each resolution. The overall results are consistent with each other and do not depend significantly on the resolution and energy. The H.E.S.S.18($E > 2$ TeV) results yield the hadronic and leptonic counts of $\sim 8\sigma$:4σ at the highest resolution, and are of somewhat higher relative sensitivity than the lower resolution results.

4. DISCUSSION ON THE GAMMA-RAY ORIGIN

4.1. *The Hybrid Origin of the Gamma Rays in a SNR*

The present analysis revealed that the gamma rays in RX J1713 consist of the hadronic components and the leptonic components with a ratio of 7 : 3 in the gamma-ray counts. This is the first result which has quantified the two gamma-ray components, and has opened a possibility to explore the physical processes operating in each part of the SNR. It is to be emphasized that the separation of the two gamma ray components was achieved for the first time only by including explicitly the ISM proton column density. The hybrid origin was theoretically modeled by ZA10 (see their Figure 14). The present results indicate that the hadronic component is more significant than shown by ZA10 which assumed a small target mass of the ISM. In fact, ZA10 assumed the interacting molecular mass to be 100–1000 $M_\odot$ which com-

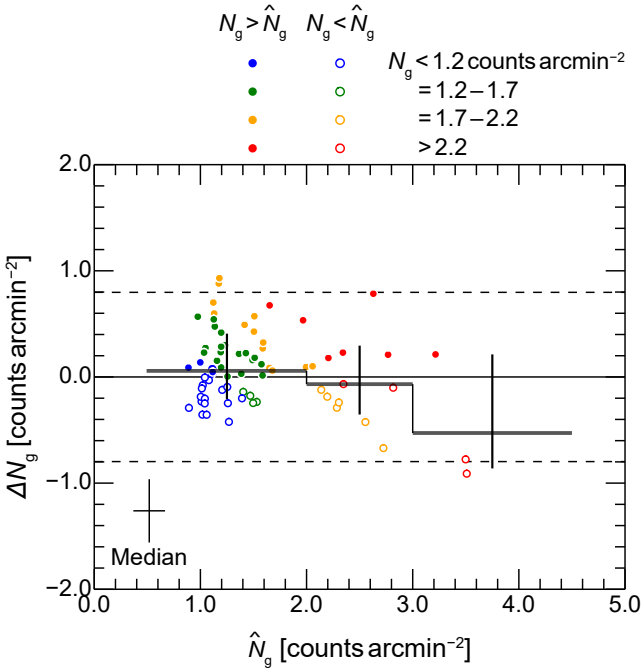


Figure 5. A plot of the difference $\Delta N_g = N_g - \hat{N}_g$ with respect to $\hat{N}_g$ derived from Equation (4) for H.E.S.S.18 ($E >$ 2 TeV) with a pixel size of 4′.8. The positive (above the horizontal dashed line) pixels and the negative pixels are shown by filled and open symbols, and the color code in N_g is the same as in Figure 4. The horizontal- and vertical error bars shown in the left bottom corner indicate the median values of $\sigma(\hat{N}_g)$ (Equation (6)) and $\sigma(\Delta N_g)$ (Equation (7)), respectively. The averages of ΔN_g weighted with $\sigma(\Delta N_g)^{-2}$ are shown for three bins of $\hat{N}_g$ with the vertical error bars. The dashed lines show the 2.5× weighted-root-mean-square of ΔN_g.

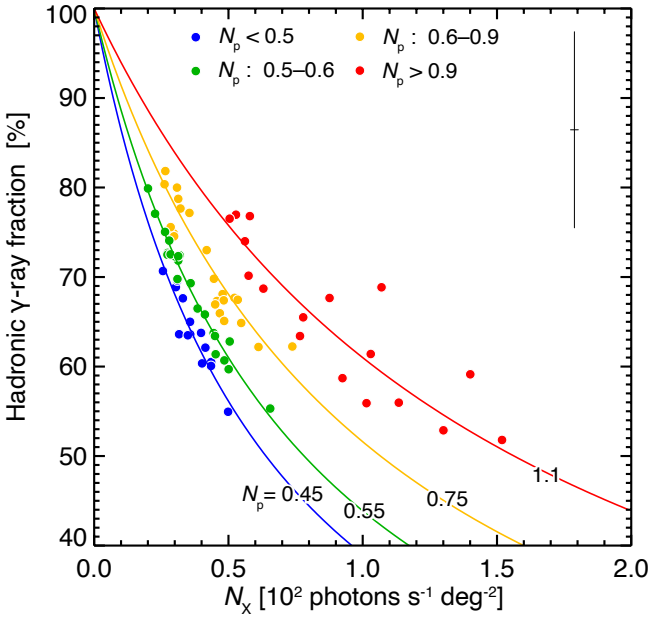


Figure 6. Scatter plot between hadronic gamma-ray fraction and N_x. The hadronic gamma-ray fraction is derived from Equation (12). Blue, green, yellow, and red circles represent the data points where N_p less than 0.5, 0.5–0.6, 0.6–0.9, and more than 0.9, respectively. Blue, green, yellow, and red solid lines show the relationships derived from Equation (12) when $N_p = 0.45, 0.55, 0.75$, and 1.1, respectively. The typical error bar for each data point is shown in the right top corner, which indicates median values of $\sigma(N_p)$ and hadronic gamma-ray fraction. The error of the hadronic gamma-ray fraction is estimated as $(aN_p/\hat{N}_g)((\sigma_a/a)^2 + (N_p/\sigma(N_p))^2 + (\hat{N}_g/\sigma(\hat{N}_g))^2)^{1/2}$.

prises only two individual molecular clouds C and D (Fukui 2008). The total ISM mass associated with the SNR, however, is amounts to ∼20,000 $M_\odot$ by summing up all molecular and atomic clouds interacting with the SNR (F12).

The principal aim of F12 was to clarify if the target protons in the hadronic process in RX J1713 show good correspondence with the interstellar protons including H I in addition to H_2. The new feature was the inclusion of H I, and the spatial correspondence is the necessary condition of the hadronic gamma rays. It was also shown by IYIF12 that the magnetic field is likely as strong as 100 mG or higher, making the leptonic component unfavorable. Their azimuthal angle distribution of the gamma rays and ISM seems to be matched without invoking an additional contribution[2]. Accordingly, F12 concluded that the gamma rays are mainly due to the hadronic origin, while the contribution of the leptonic component was not excluded. The subsequent works on CTA simulations of the hadronic and leptonic origins pursued this issue and argued for a possibility of resolving the degeneracy originating by the shell-like distribution of the ISM and nonthermal X-rays (Acero et al. 2017). In the other two TeV gamma ray SNRs, HESS J1731−347 and RCW 86, the ISM and the nonthermal X-rays show significantly different spatial distributions, allowing one to separate the two origins (Fukuda et al. 2014; Sano et al. 2019), while the other TeV gamma ray SNR RX J0852.0−4622 shows shell-like distributions of the ISM and nonthermal X-rays, making a case similar to RX J1713. In order to shed more light

[2] We note that in their Figure 8(b) large deviations are found at 15° and 165° in azimuth angle in their Section 3.5.2. 115° is to be corrected to 15°, see the erratum.

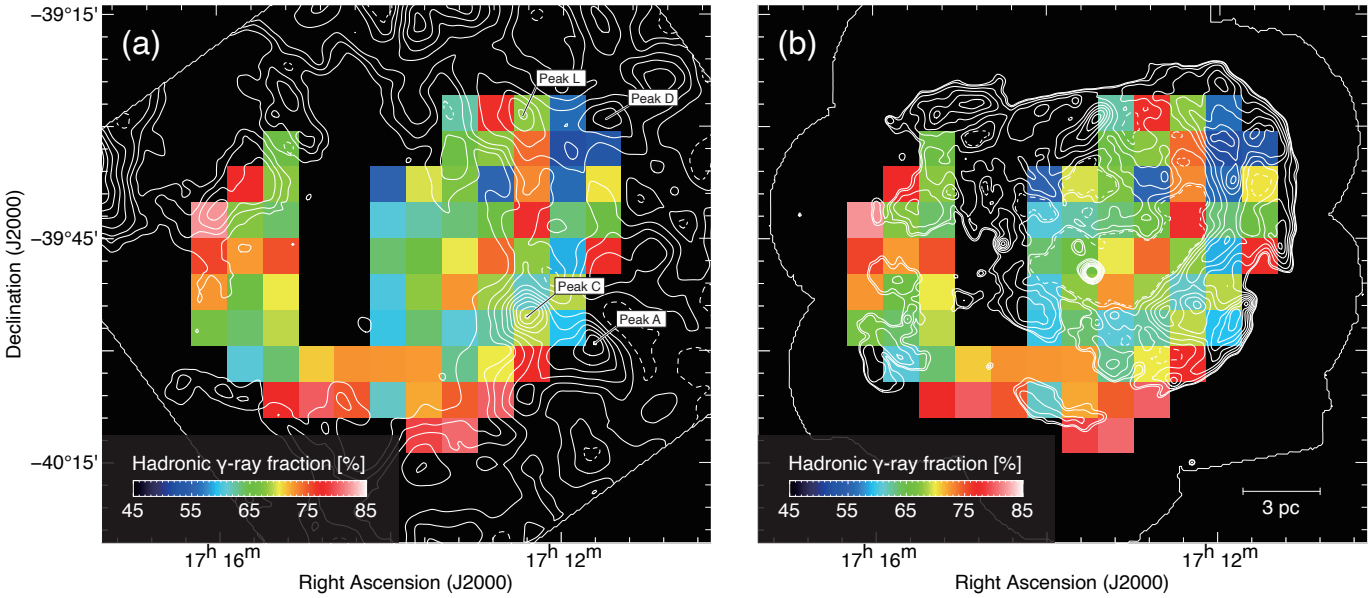


Figure 7. Distributions of hadronic gamma-ray fraction overlaid with (a) total proton column density $N_{\rm p}({\rm H_2+H\,I})$ (F12) and (b) *XMM-Newton* X-rays (E: 1.0–5.0 keV). The contour levels are the same as shown in Figure 3. The prominent dense clumps Peak A, C, D, and L are also indicated.

on the issue we applied the present method to the previous data H.E.S.S.07 used by F12, and find that the ratio of the hadronic component and the leptonic components is $\sim(72 \pm 11) : (28 \pm 10)$ in gamma-ray count, which is similar to the present results. The 3σ significance of the leptonic component might place it at a marginal level, while the low spatial resolution and the small number of the data pixels would make the analysis of H.E.S.S.07 crude at best.

4.2. *Possible Suppression of the Gamma Rays by the 2nd Order Effects*

A further issue is the possible suppression of the gamma rays by the 2nd order effects that may make the gamma rays deviate from a simple proportionality to $N_{\rm p}$ or $N_{\rm x}$. Such effects include the shock cloud interaction and the penetration depth. Some other effects like secondary particle acceleration may be operating as suggested by Aharonian (2004), while these effects are not yet fully investigated/confirmed theoretically or observationally; such mechanisms include the 2nd order Fermi acceleration (Fermi 1949), magnetic reconnection in the turbulent medium (Hoshino 2012), reverse shock acceleration (e.g., Ellison 2001), and non-liner effect of DSA (e.g., Malkov & Drury 2001). We shall not discuss them in the present paper.

IYIF12 made MHD numerical simulations of the shock front interacting with the clumpy ISM. Recent MHD simulations of the dense cores overtaken by the shock by Celli et al. (2019) for more realistic core density higher than that of IYIF12 confirmed the results of IYIF12. The interaction produces highly turbulent velocity field around the dense cores, which amplifies the magnetic field up to 100 μG–1 mG. The effects are observationally confirmed by the rim-brightened X-rays for a typical radius of the dense cores 0.5 pc by Sano et al. (2013) through a detailed comparative study of the ISM and X-rays. The $\sim$100 μG B field will deplete CR electrons by synchrotron cooling and can lead to suppression of the leptonic gamma rays.

In the hadronic origin, the gamma rays are not always perfectly proportional to the ISM column density because CRs cannot penetrate freely into the dense cores as pointed out by Gabici et al. (2007) and IYIF12. The expression of the penetration depth of CR protons into dense cores is given as follows (IYIF12);

$$l_{\rm pd}\ ({\rm pc}) = 0.1\ \eta^{1/2} \left(\frac{E}{10\,{\rm TeV}}\right)^{1/2} \times \left(\frac{B}{100\,\mu G}\right)^{-1/2} \left(\frac{t_{\rm age}}{10^3\,{\rm yr}}\right), \qquad (13)$$

where $l_{\rm pd}$ is the penetration depth of cosmic rays, η is the CR gyro-factor, E is the cosmic-ray energy, B is the magnetic field strength, and $t_{\rm age}$ is the age of the SNR. If we adopt $E = 10\,{\rm TeV}$[3], $t_{\rm age} = 1600\,{\rm yr}$, $B = 100\,\mu{\rm G}$

[3] The gamma-ray images used for the represent paper correspond to the CR proton energy $\sim$3–20 TeV, which is roughly an order of magnitude higher than the lower energy threshold of the images.

(Celli et al. 2019), and $\eta = 1$ (e.g., Tanaka et al. 2008; Tsuji et al. 2019), we estimate $l_{\rm pd} = 0.13\,{\rm pc}$. The dense cores in RX J1713 have a typical radius of $\sim 0.5\,{\rm pc}$ (Sano et al. 2010, 2013) and $l_{\rm pd}$ is small enough to affect the CR injection into the dense cores. Here, the volume filling factor of the dense cores in RX J1713 is ∼10% by assuming 22 molecular clouds with typical radii of ∼1.4 pc and the SNR shell radius of 9 pc (Sano et al. 2013). The gamma ray suppression is therefore not likely to be dominant overall.

Recently, Sano et al. (2020) revealed high resolution distribution of CO with ALMA toward part of the peak D cloud, and small-scale (0.1–0.02 pc) clumpy distribution has been revealed. If such a highly clumpy distribution is common in the ISM, CRs may more easily penetrate into dense ISM and may increase the hadronic gamma rays more than inferred from unresolved ISM distribution. So, it will be important to resolve the ISM at a sub-pc scale in order to better understand the hadronic gamma rays.

In either case, the suppression is supposed to appear at high $N_{\rm g}$, and the slight decrease of $\Delta N_{\rm g}$ in only three pixels at around 2.5 σ level in Figure 5 might be caused by these effects. The three pixels are indicated by green lines in Figure 1(a). This issue is to be clarified by future more sensitive observations. Overall, the present methodology appears to describe the general behaviour of $N_{\rm g}$.

4.3. *Prospect to Improve Accuracy of the ISM Column Density*

The present work used the ISM distribution consisting of both atomic and molecular hydrogen (F12). A problem we faced is that the accuracy of estimating N(H I) is limited by the H I self-absorption. By new identification of possible self-absorption H I, we excluded 18 pixels from the analysis, where self-absorption effects are suspected. Since the accuracy in correction for the self-absorption is limited by the uncertainty in the assumed H I background emission, it is impossible to achieve accuracy better than ∼20% for a correlation analysis if self-absorption is significant. If the correction is not adequate in some pixels of the present analysis, it leads to underestimate the ISM column density and $\hat{N}_{\rm g}$ as well. Then, $\Delta N_{\rm g}$ becomes overestimated in Figure 5. The four pixels with deviation more than 2.5σ in a range of $\hat{N}_{\rm g} = 1.0$–2.0 may show such a case. In order to correct such inaccuracies, we need to develop a new tracer both for H I and H_2. Inoue & Inutsuka (2012) made numerical simulations of magneto-hydrodynamics of colliding H I flows and traced the H I evolution leading to H_2 cloud formation. By synthetic observations of the numerical results of Inoue & Inutsuka (2012), Tachihara et al. (2018) and Fukui et al. (2018) show that the submm transition of neutral carbon C I is a good tracer of the whole ISM protons (H I+H_2) in a density regime around 10^3 cm^{-3} (see Figure 8 of Tachihara et al. 2018). We suggest that C I serves as a useful probe of ISM protons in future and may become a promising tool in a ISM study of SNRs. This is particularly relevant in the CTA era, where more SNRs in the Galactic plane, subject to strong H I absorption, will be discovered.

4.4. *The SNR Evolution in the Last 1600 yr*

Once a SNe occurs, CRs are accelerated by the DSA in the SNR. Non-thermal X-rays are emitted by the synchrotron mechanism, and the gamma rays by the p-p reaction or the inverse Compton scattering. A general picture of the hadronic and leptonic gamma rays from a non-thermal X-ray SNR is that the gamma rays are proportional to either $N_{\rm p}$ or $N_{\rm x}$. In RX J1713, the CRs are perturbed by the interaction with the ISM. The distribution of the ISM is highly clumpy with the dense cores having a small volume filling factor of ∼10% in RX J1713. The distribution was determined prior to the SNe by the cloud self-gravity which may involve star formation as in the peak C (Sano et al. 2010) and the environmental effects including the progenitor's stellar winds over Myr. The theoretical studies of the interaction show that the gamma rays and X-rays are significantly affected by the dense cores (Gabici et al. 2007; IYIF12; Celli et al. 2019). The secondary acceleration of CRs might also affect the X-rays as suggested by a spectral analysis of X-rays by Sano et al. (2015), whereas there is no established picture on the acceleration.

The present hybrid picture is qualitatively consistent with the composite scenario by ZA10. Naturally, the fraction of the leptonic gamma rays increases where the ISM density is low. In the other three TeV gamma ray SNRs, HESS J1731−347 (HESS J1731), RX J0852.0−4622, and RCW86, spatial correspondence between the gamma rays and the ISM has been shown and the hadronic gamma rays are suggested to be dominant (Fukuda et al. 2014; Fukui et al. 2017; Sano et al. 2019). In two of them, HESS J1731 and RCW86, in a minor portion of the SNRs where the gamma-ray distribution shows correspondence with the nonthermal X-rays but not with the ISM, it is suggested that the gamma rays are mostly of the leptonic origin (Fukuda et al. 2014; Sano et al. 2019). RX J1713 is a more complicated case where the non-thermal X-rays are heavily overlapped with the gamma rays and are not easily separable at the current resolution. The methodology proposed in the present work has opened a new tool to

quantify the leptonic and hadronic gamma rays and will be applicable to the other SNRs. The present paper lends support for the vital role of the ISM in the production of the HE and VHE energy radiations in a SNR, confirming that the inclusion of the ISM in an analysis is crucial for our understanding the origin of the gamma rays.

Furthermore, numerical simulations of the gamma ray SEDs in RX J1713 have been made by ZA10 as well as the other authors (see references in ZA10). These simulations assumed the ratio of relativistic electrons to protons $K_{\rm ep}$ of 10^{-2} to 10^{-3} and obtained results which are not inconsistent with the present result. This suggests that the assumed values above satisfy the present requirement of the gamma-ray and X-ray results in addition to the ISM data, whereas it seems that better statistics of the gamma-ray data, which will be provided in the CTA era, would enable us to better constrain $K_{\rm ep}$.

5. CONCLUSIONS

In order to pursue the origin of the gamma rays in the SNR RX J1713.7−3946 (RX J1713) we have carried out a comparative study of the H.E.S.S. TeV gamma rays with the ISM protons and the non-thermal X-rays. The main conclusions of the present work are summarized as follows.

1. We propose a new methodology which assumes that the gamma-ray counts $N_{\rm g}$ is expressed by a linear combination of two terms; one is proportional to the ISM column density Np and the other proportional to the X-ray count $N_{\rm x}$. By fitting the expression to the data pixels, we find that the gamma-ray counts are well represented by a tilted flat plane in a 3D space of $N_{\rm p}$-$N_{\rm x}$-$N_{\rm g}$. This plane illustrates that the total gamma rays $N_{\rm g}$ increases with $N_{\rm p}$ and $N_{\rm x}$, respectively, which is consistent with the hybrid picture. The fitting is robust with the goodness of fitting $R^2 = 0.92$ close to a complete fit with $R^2 = 1.0$. The results show that the hadronic and leptonic components occupy (58–70)% and (25–37)% of the total gamma rays, respectively. The two components have been quantified for the first time by the methodology. The hadronic component is typically by a factor of ∼2 greater than the leptonic component, especially as yielded by the highest resolution dataset at >2 TeV. The dominance of the hadronic gamma rays reflects the massive ISM of $\sim 10^4\ M_\odot$, target protons in the p-p reaction, associated with the SNR (F12), lending further support for the acceleration of the cosmic-ray protons.

2. The theoretical broad band fit to the gamma-ray and X-ray spectra shows it likely that the leptonic gamma rays are existent in RX J1713 as well as the hadronic gamma rays. The new methodology has opened a possibility of a pixel-resolved analysis by the broad-band gamma-ray and X-ray spectral fitting as a next step. F12 showed that the ISM distribution has a good spatial correspondence to the gamma rays, and suggested that it supports the production of the hadronic gamma rays. The contribution of the leptonic gamma rays was, however, not quantified in the previous observational studies in part due to the degeneracy of the two components of the similar shell-like distribution (Aharonian et al. 2007; H. E. S. S. Collaboration 2018; F12). The nonsignificant contribution of the leptonic component in F12 may be ascribed to the low photon counts of the previous H.E.S.S. dataset in 2007 and the low resolution ∼10′ employed by F12.

3. There is a marginal hint that the gamma rays are suppressed at high gamma-ray counts which may be ascribed to the second order effects including the shock-cloud interaction and the penetration-depth effect. The shock-cloud interaction excites turbulence toward the dense cores and amplifies the turbulent magnetic field up to 100 μG. The strong field deceases the CR electrons by the synchrotron cooling, leading to suppress the leptonic gamma rays by the inverse Compton scattering. In addition, the CR protons cannot penetrate into the dense cores because of the limited penetration depth around the dense cores where the turbulent magnetic field reduces the CR diffusion. This reduces the hadronic gamma rays toward the dense cores. These two effects will suppress the gamma rays toward the dense cores. In the CTA observations at high resolution, the two effects may become more significant than shown here.

4. The present analysis employed the H I data corrected for the self-absorption, whereas in some region of the SNR the accuracy in the correction may be limited due to difficulty in estimating the background H I emission. This can be an obstacle in future applications of the methodology to distant SNRs in the Galaxy, where stronger H I absorption is expected. We suggested that the C I sub-mm transition can be better used as a promising tracer of the whole ISM protons of both atomic and molecular hydrogen, which may help to improve the accuracy in the ISM column den-

sity. The development of such new probes will be crucial in future studies of the gamma ray origins. ALMA is obviously a powerful high resolution instrument of C I observations and NANTEN2 will provide a large-scale view of C I distribution by determining a X_{CI} factor for converting W(C I) into N_H. The combination of the two with CTA will greatly facilitate the accurate measurements of the interstellar protons.

ACKNOWLEDGMENTS

We are grateful to the anonymous referee for his/her valuable comments on an earlier version of the manuscript that greatly improved the manuscript. The NANTEN project is based on a mutual agreement between Nagoya University and the Carnegie Institution of Washington (CIW). We greatly appreciate the hospitality of all the staff members of the Las Campanas Observatory of CIW. We are thankful to many Japanese public donors and companies who contributed to the realization of the project. This work is financially supported by a grant-in-aid for Scientific Research (KAKENHI, Nos. 24224005, 15H05694, 19H05075, 20H01944, and 21H01136) from MEXT (the Ministry of Education, Culture, Sports, Science and Technology of Japan).

Facilities: ALMA, H.E.S.S., NANTEN

APPENDIX

A. DISTANCE DETERMINATION OF RX J1713

In the Galactic plane, accurate determination of distance to a SNR generally involves large uncertainty, since SNRs have no clear correlation between the observed size and radio brightness. It is often the case that the kinematic distance offers a reliable distance once an association between a SNR and the interstellar clouds is established. In case of RX J1713, there seems to be some issues concerning the method of distance estimate in the literature. We will review the previous work, and clarify the background of the present study.

The SNR RX J1713 was first identified by Pfeffermann & Aschenbach (1996) by ROSAT at 1′–6′ resolution in the X-ray energy range of 0.1–2.5 keV, and the X-ray spectrum was interpreted to be thermal. They derived X-ray absorption column density to be (3–12) $\times 10^{21}$ cm^{-2} for an effective resolution of $\sim 17'$. Koyama et al. (1997) made X-ray observations with ASCA in a range of 0.7–10.0 keV, which covered the northwestern shell with the FoVs of $22' \times 22'$ square (SIS) and a circular shape with a diameter of 50′ (GIS). These authors derived the average absorption column density of the shell region to be (4.8–10.1)$\times 10^{21}$ cm^{-2} from X-rays. The absorption occurs at low energy less than 1 keV, and the two works yielded similar average column densities. Pferffermann and Aschenbach estimated the distance to be 1 kpc by fitting a Sedov model. Koyama et al. (1997) also derived a distance of 1 kpc of the SNR corresponding to the average column density. These works assumed the gas distribution is uniform in the Galactic disk, and referred to the total column density to the Galactic center, 6×10^{22} cm^{-2}, which is roughly ten times higher than that derived by them. This assumption however turned out to be incorrect in two ways later. First, the gas in the disk toward RX J1713 is far from uniform and there is a significant decrease of hydrogen column density, which is

seen as a hole of CO (see below). Second, most of the absorption is caused within the SNR and is not proportional to distance; Sano et al. (2015) showed that the X-ray absorption is divided into that within the SNR and that in a single foreground discrete cloud, where their ratio is 7 : 3 (see Figure 7a of Sano et al. 2015).

Subsequently, Slane et al. (1999) found that the interstellar gas has a hole toward the SNR by chance, raising a doubt on an assumption of uniform column density. These authors inspected CO distribution in the CfA survey at 9′ resolution (Bronfman et al. 1989) and found that clouds at -94–-69 km s^{-1} show spatial correspondence with the SNR. For these clouds, they derived a kinematic distance of 6 kpc by using the Galactic rotation curve. However, F03 used the NANTEN CO survey and identified that another cloud at -10 km s^{-1} shows good correspondence with the SNR at a higher resolution of 2′.6 with a higher sensitivity. These authors thus derived a kinematic distance to be 1 kpc and Moriguchi et al. (2005) supported the distance by presenting a full account of the NANTEN CO data in the region. Soon after, Cassam-Chenaï et al. (2004) confirmed the correspondence of the spatially varying X-ray absorption with the H I and CO, and argued for a distance of 1.3 kpc. The readers are able to refer to a full account of the X-ray absorption, which varies mainly over a large range of 0.4–1.4 $\times$ 10^{22} cm^{-2} in column density, in Sano et al. (2015) based on the Suzaku X-ray data. The distance is supported by a number of subsequent works on the association of the -10 km s^{-1} cloud with the SNR (e.g., Acero et al. 2009; Sano et al. 2010, 2013, 2015; Tanaka et al. 2020), and seems to be confirmed by the recent GAIA data (Leike et al. 2021).

In summary, the distance of RX J1713, 1 kpc, is established based on the association of the -10 km s^{-1} cloud with the SNR (F03; Cassam-Chenaï et al. 2004; Moriguchi et al. 2005). A similar estimate of 1 kpc by the early X-ray works (e.g., Koyama et al. 1997) was fortuitous due to an incorrect assumption of uniform column density in the Galactic disk.

B. X-RAY ABSORPTION BY THE ISM

It is well known that X-ray emission can be absorbed by the ISM which is located between the X-ray emitting source and observer. Considering the energy-dependent photoionization cross section of the ISM, the X-ray absorption becomes significant in the soft X-ray band generally below 1 keV when the ISM column density is $\sim$10^{22} cm^{-2} (e.g., Balucinska-Church & McCammon 1992). Since the typical absorbing column densities of RX J1713 is $\sim$0.4–1.0 $\times$ 10^{22} cm^{-2} by X-ray spectroscopies, soft-band X-ray images might be affected by the interstellar absorption (e.g., Cassam-Chenaï et al. 2004; Sano et al. 2015; Okuno et al. 2018). In this section, we shall test which energy bands of X-ray images are free for the interstellar absorption in RX J1713.

Figure 8 shows exposure-corrected background-subtracted X-ray flux images in energy bands of 0.5–0.8, 0.8–1.0, 1.0–2.0, 2.0–3.0, and 3.0–5.0 keV. We find that three X-ray images of 1.0–2.0, 2.0–3.0, and 3.0–5.0 keV show similar spatial distributions to each other. On the other hand, 0.5–0.8 and 0.8–1.0 keV images are significantly different with the others especially for the southern part of the shell. The X-ray depression in soft-band images is likely caused by the interstellar absorption of foreground local clouds, which was previously mentioned by Moriguchi et al. (2005) and Sano et al. (2015).

To evaluate the absorption effect in the soft band X-ray images, we calculated hardness ratios HR which provides a photometric color index by a following equation using high-energy band image H and low-energy band image S;

$$\mathrm{HR} = (H - S)/(H + S). \tag{B1}$$

In the present study, we fixed high-energy band image H to 3.0–5.0 keV image for the reference and normalized the hardness ratio whose Gaussian center will be adjusted to zero.

Figure 9 shows histograms of normalized hardness ratios within the SNR shell for each low-energy band images. We find the dispersions of histograms for 1.0–2.0 and 2.0–3.0 keV are narrow, whereas the other two soft bands below 1 keV show wider dispersions. The dispersion (full-width half-maximum) obtained by a Gaussian fitting is 0.37 for 0.5–0.8 keV, 0.45 for 0.8–1.0 keV, 0.22 for 1.0–2.0 keV, and 0.22 for 2.0–3.0 keV. Since the dispersion reflects intensity variations of an X-ray image due to the interstellar absorption, we conclude that X-ray images of 1 keV or higher energy could be considered as the absorption free or neglectable in RX J1713. We therefore used the 1.0–5.0 keV image for the correlation study.

C. MULTIPLE LINEAR REGRESSION

We have made a weighted least-squares estimation of the coefficients in Eqation (4) and their standard error, goodness-of-fit tests, and reda diagnostic of multicollinearity, according to Chapters 6, 10 and 11 of Kutner et al. (2005).

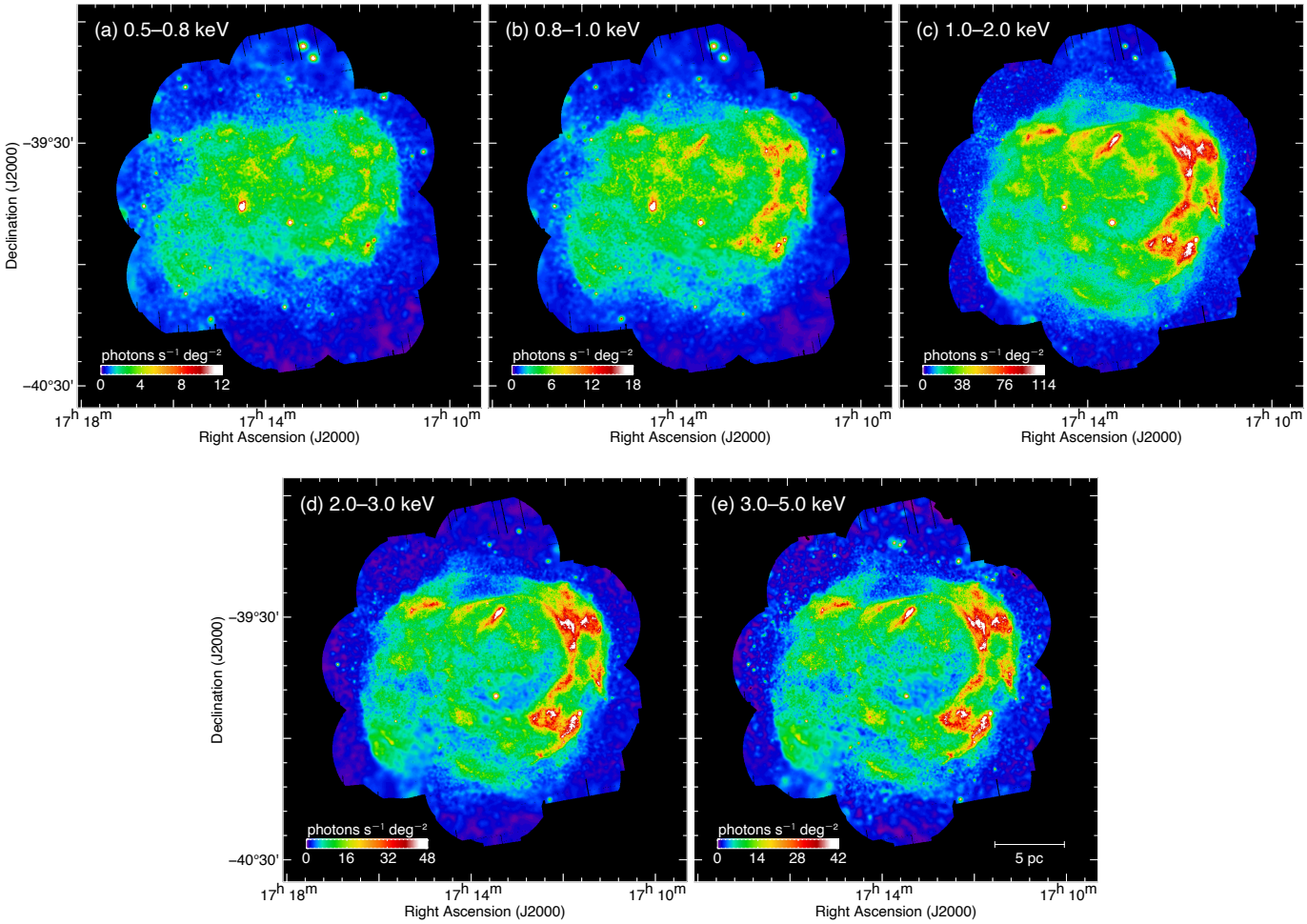


Figure 8. Exposure-corrected background-subtracted X-ray flux images in energy bands of (a) 0.5–0.8 keV, (b) 0.8–1.0 keV, (c) 1.0–2.0 keV, (d) 2.0–3.0 keV, and (e) 3.0–5.0 keV. The scale bar is also shown in the bottom right corner in Panel (e).

C.1. *Estimation of the Regression Coefficients*

Equation (4) can be rewritten in a matrix form

$$\begin{pmatrix} N_{\mathrm{g},1} \\ \vdots \\ N_{\mathrm{g},n} \end{pmatrix} = \begin{pmatrix} N_{\mathrm{p},1} & N_{\mathrm{x},1} \\ \vdots & \vdots \\ N_{\mathrm{p},n} & N_{\mathrm{x},n} \end{pmatrix} \begin{pmatrix} a \\ b \end{pmatrix} + \begin{pmatrix} \varepsilon_1 \\ \vdots \\ \varepsilon_n \end{pmatrix}, \tag{C2}$$

or more simply

$$\mathbf{y} = \mathbf{X}\mathbf{b} + \boldsymbol{\varepsilon}, \tag{C3}$$

where $\mathbf{y} = (\ N_{\mathrm{g},1}\ \cdots\ N_{\mathrm{g},n}\ )^{\mathrm{T}}$ is a vector of n observations on the dependent variable N_{g} and the superscript T means transpose,

$$\mathbf{X} = \begin{pmatrix} N_{\mathrm{p},1} & N_{\mathrm{x},1} \\ \vdots & \vdots \\ N_{\mathrm{p},n} & N_{\mathrm{x},n} \end{pmatrix}$$

is an $n \times 2$ matrix where we have observations on two explanation variables, N_{p} and N_{x}, for n observations, $\mathbf{b} = (\ a\ \ b\ )^{\mathrm{T}}$ is a vector of unknown coefficients which we want to estimate and $\boldsymbol{\varepsilon} = (\ \varepsilon_1\ \cdots\ \varepsilon_n\ )^{\mathrm{T}}$ is a vector of disturbances.

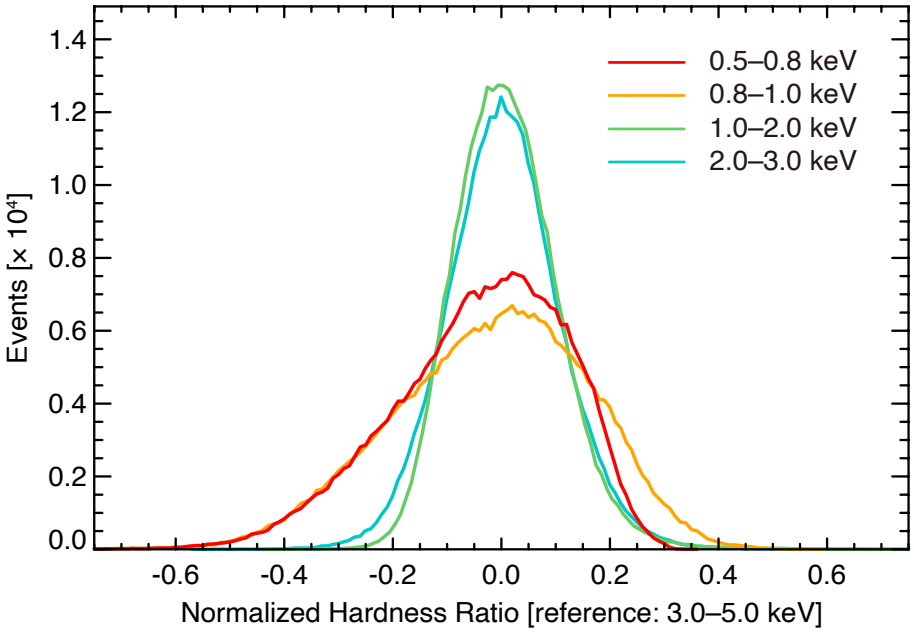


Figure 9. Histograms of normalized hardness ratios respect to the energy band of 3.0–5.0 keV. The data was extracted from inside the shell eclipse centered at ($\alpha_{\rm J2000}$, $\delta_{\rm J2000}$) = ($17^{\rm h}13^{\rm m}42\overset{\rm s}{.}0$, $-39^\circ45'36\overset{''}{.}0$), whose semimajor and semiminor radii are $0\overset{\circ}{.}55$ and $0\overset{\circ}{.}48$ with a position angle of -51°.

An estimate of the coefficients $\hat{\mathbf{b}}$ which minimize the sum of squared residuals $\boldsymbol{\varepsilon}^{\rm T}\boldsymbol{\varepsilon}$ is given as

$$\hat{\mathbf{b}} = (\mathbf{X}^{\rm T}\mathbf{W}\mathbf{X})^{-1}\mathbf{X}^{\rm T}\mathbf{W}\mathbf{y}, \tag{C4}$$

where an $n \times n$ diagonal matrix

$$\mathbf{W} = \begin{pmatrix} w_1 & & \\ & \ddots & \\ & & w_n \end{pmatrix}$$

is the weight matrix, $w_i = \sigma(N_{{\rm g},i})^{-2}$ $(i = 1 \cdots n)$. Here, we do not take into account $\sigma(N_{\rm p})$ and $\sigma(N_{\rm x})$ because they are relatively small; $\sigma(N_{\rm p})/N_{\rm p} = 10^{-2}$ and $\sigma(N_{\rm x})/N_{\rm x} = 10^{-2}$–$10^{-3}$, while $\sigma(N_{\rm g})/N_{\rm g} = 10^{-1}$. The standard error of the estimated coefficients, σ_a and σ_b, are given as the square root of the diagonal elements of a matrix

$$\frac{(\mathbf{y} - \hat{\mathbf{y}})^{\rm T}\mathbf{W}(\mathbf{y} - \hat{\mathbf{y}})}{n - m}(\mathbf{X}^{\rm T}\mathbf{W}\mathbf{X})^{-1}, \tag{C5}$$

where $\hat{\mathbf{y}} = \mathbf{X}\hat{\mathbf{b}} = (\ \hat{N}_{{\rm g},1}\ \cdots\ \hat{N}_{{\rm g},n}\ )^{\rm T}$ is a vector of predicted values of $N_{\rm g}$ and $m = 2$ is the number of explanation variables ($N_{\rm p}$ and $N_{\rm x}$).

C.2. *Goodness-of-Fit Measure and F-Test*

Taking into account the particularities of regression through the origin (briefly summarized in Appendix A of Legendre & Desdevises 2009), we calculate the coefficient of determination[4] as

$$R^2 = \sum_{i=1}^{n}(\hat{N}_{{\rm g},i})^2 \Big/ \sum_{i=1}^{n}(N_{{\rm g},i})^2 \tag{C6}$$

and F-statistic associated with R^2 as

$$F = \frac{R^2/m}{(1 - R^2)/(n - m)}. \tag{C7}$$

[4] According to Kvålseth (1985), there are eight types of definitions of R^2. Equation (C6) corresponds to Equation (8) of this author.

R^2 indicates how the variance in the dependent variable ($N_{\rm g}$) can be explained by those in the explanation variables. It normally ranges from 0 to 1 and a high R^2 indicates a good fit. The derived $F = 337.0$ is much greater than the critical value of the F-distribution with $(m,\, n-m)$ degrees of freedom, $F_{0.01}(2, n-2) = 4.9$, therefore we can reject a null-hypothesis $a = b = 0$ which means $N_{\rm g}$ is dependent on neither $N_{\rm p}$ nor $N_{\rm x}$, at a significance level of 1%.

C.3. *Diagnostics of Multicollinearity*

red Multicollinearity is a well known problem which increases the variance of the coefficient estimates (σ_a and σ_b in the present study) and makes the estimates unstable. It occurs when the explanation variables in the regression model are highly correlated. A formal and widely accepted method for detectidng the presence of multicollinearity is use of variance inflation factor (VIF). A VIF value greater than 10 is commonly used as an indicator of multicollinearity but a more conservative threshold of 5 or 3 is sometimes chosen.

red There are only two explanation variables ($N_{\rm p}$ and $N_{\rm x}$) in the regression model in the present study, the VIF is given by

$$\mathrm{VIF} = \frac{1}{1-r^2}, \tag{C8}$$

where r is the correlation coefficient between $N_{\rm p}$ and $N_{\rm x}$. The correlation coefficient of $r = 0.71$ – 0.80 give VIF of 2.0 – 2.8 which are in an acceptable range.

REFERENCES

Abdo, A. A., Ackermann, M., Ajello, M., et al. 2011, ApJ, 734, 28, doi: 10.1088/0004-637X/734/1/28

Acero, F., Ballet, J., Decourchelle, A., et al. 2009, A&A, 505, 157, doi: 10.1051/0004-6361/200811556

Acero, F., Aloisio, R., Amans, J., et al. 2017, ApJ, 840, 74, doi: 10.3847/1538-4357/aa6d67

Aharonian, F., Akhperjanian, A. G., Bazer-Bachi, A. R., et al. 2006, A&A, 449, 223, doi: 10.1051/0004-6361:20054279

—. 2007, A&A, 464, 235, doi: 10.1051/0004-6361:20066381

Aharonian, F. A. 2004, Very high energy cosmic gamma radiation : a crucial window on the extreme Universe (World Scientific), doi: 10.1142/4657

Aharonian, F. A., Atoyan, A. M., & Kifune, T. 1997, MNRAS, 291, 162, doi: 10.1093/mnras/291.1.162

Aharonian, F. A., Drury, L. O., & Voelk, H. J. 1994, A&A, 285, 645

Aharonian, F. A., Akhperjanian, A. G., Aye, K. M., et al. 2004, Nature, 432, 75, doi: 10.1038/nature02960

Balucinska-Church, M., & McCammon, D. 1992, ApJ, 400, 699, doi: 10.1086/172032

Bell, A. R. 1978, MNRAS, 182, 147, doi: 10.1093/mnras/182.2.147

Bertsch, D. L., Dame, T. M., Fichtel, C. E., et al. 1993, ApJ, 416, 587, doi: 10.1086/173261

Blandford, R. D., & Ostriker, J. P. 1978, ApJL, 221, L29, doi: 10.1086/182658

Bronfman, L., Alvarez, H., Cohen, R. S., & Thaddeus, P. 1989, ApJS, 71, 481, doi: 10.1086/191384

Cassam-Chenaï, G., Decourchelle, A., Ballet, J., et al. 2004, A&A, 427, 199, doi: 10.1051/0004-6361:20041154

Celli, S., Morlino, G., Gabici, S., & Aharonian, F. A. 2019, MNRAS, 487, 3199, doi: 10.1093/mnras/stz1425

Drury, L. O., Aharonian, F. A., & Voelk, H. J. 1994, A&A, 287, 959. https://arxiv.org/abs/astro-ph/9305037

Ellison, D. C. 2001, SSRv, 99, 305

Ellison, D. C., Patnaude, D. J., Slane, P., & Raymond, J. 2010, ApJ, 712, 287, doi: 10.1088/0004-637X/712/1/287

Fermi, E. 1949, Physical Review, 75, 1169, doi: 10.1103/PhysRev.75.1169

Fukuda, T., Yoshiike, S., Sano, H., et al. 2014, ApJ, 788, 94, doi: 10.1088/0004-637X/788/1/94

Fukui, Y. 2008, in American Institute of Physics Conference Series, Vol. 1085, American Institute of Physics Conference Series, ed. F. A. Aharonian, W. Hofmann, & F. Rieger, 104–111

Fukui, Y., Hayakawa, T., Inoue, T., et al. 2018, ApJ, 860, 33, doi: 10.3847/1538-4357/aac16c

Fukui, Y., Torii, K., Onishi, T., et al. 2015, ApJ, 798, 6, doi: 10.1088/0004-637X/798/1/6

Fukui, Y., Moriguchi, Y., Tamura, K., et al. 2003, PASJ, 55, L61, doi: 10.1093/pasj/55.5.L61

Fukui, Y., Sano, H., Sato, J., et al. 2012, ApJ, 746, 82, doi: 10.1088/0004-637X/746/1/82

Fukui, Y., Okamoto, R., Kaji, R., et al. 2014, ApJ, 796, 59, doi: 10.1088/0004-637X/796/1/59

Fukui, Y., Sano, H., Sato, J., et al. 2017, ApJ, 850, 71, doi: 10.3847/1538-4357/aa9219

Gabici, S., & Aharonian, F. A. 2014, MNRAS, 445, L70, doi: 10.1093/mnrasl/slu132

Gabici, S., Aharonian, F. A., & Blasi, P. 2007, Ap&SS, 309, 365, doi: 10.1007/s10509-007-9427-6

Gabriel, C., Denby, M., Fyfe, D. J., et al. 2004, in Astronomical Society of the Pacific Conference Series, Vol. 314, Astronomical Data Analysis Software and Systems (ADASS) XIII, ed. F. Ochsenbein, M. G. Allen, & D. Egret, 759

H. E. S. S. Collaboration. 2018, A&A, 612, A6, doi: 10.1051/0004-6361/201629790

Hoshino, M. 2012, PhRvL, 108, 135003, doi: 10.1103/PhysRevLett.108.135003

Inoue, T., & Inutsuka, S.-i. 2012, ApJ, 759, 35, doi: 10.1088/0004-637X/759/1/35

Inoue, T., Yamazaki, R., Inutsuka, S.-i., & Fukui, Y. 2012, ApJ, 744, 71, doi: 10.1088/0004-637X/744/1/71

Katsuda, S., Acero, F., Tominaga, N., et al. 2015, ApJ, 814, 29, doi: 10.1088/0004-637X/814/1/29

Koyama, K., Kinugasa, K., Matsuzaki, K., et al. 1997, PASJ, 49, L7, doi: 10.1093/pasj/49.3.L7

Kuntz, K. D., & Snowden, S. L. 2008, A&A, 478, 575, doi: 10.1051/0004-6361:20077912

Kutner, M. H., Nachtsheim, C. J., Neter, J., & Li, W. 2005, Applied Linear Statistical Models, 5th edn. (McGraw-Hill Irwin)

Kvålseth, T. O. 1985, The American Statistician, 39, 279

Legendre, P., & Desdevises, Y. 2009, Journal of Theoretical Biology, 259, 727

Leike, R., Celli, S., Krone-Martins, A., et al. 2021, Nature Astronomy, doi: 10.1038/s41550-021-01344-w

Malkov, M. A., & Drury, L. O. 2001, Reports on Progress in Physics, 64, 429, doi: 10.1088/0034-4885/64/4/201

McClure-Griffiths, N. M., Dickey, J. M., Gaensler, B. M., et al. 2005, ApJS, 158, 178, doi: 10.1086/430114

Moriguchi, Y., Tamura, K., Tawara, Y., et al. 2005, ApJ, 631, 947, doi: 10.1086/432653

Ogawa, H., Mizuno, A., Hoko, H., Ishikawa, H., & Fukui, Y. 1990, International Journal of Infrared and Millimeter Waves, 11, 717, doi: 10.1007/BF01010041

Okuno, T., Tanaka, T., Uchida, H., Matsumura, H., & Tsuru, T. G. 2018, PASJ, 70, 77, doi: 10.1093/pasj/psy072

Pfeffermann, E., & Aschenbach, B. 1996, in Roentgenstrahlung from the Universe, ed. H. U. Zimmermann, J. Trümper, & H. Yorke, 267–268

Planck Collaboration. 2014, A&A, 571, A11, doi: 10.1051/0004-6361/201323195

Sano, H., Sato, J., Horachi, H., et al. 2010, ApJ, 724, 59, doi: 10.1088/0004-637X/724/1/59

Sano, H., Tanaka, T., Torii, K., et al. 2013, ApJ, 778, 59, doi: 10.1088/0004-637X/778/1/59

Sano, H., Fukuda, T., Yoshiike, S., et al. 2015, ApJ, 799, 175, doi: 10.1088/0004-637X/799/2/175

Sano, H., Rowell, G., Reynoso, E. M., et al. 2019, ApJ, 876, 37, doi: 10.3847/1538-4357/ab108f

Sano, H., Inoue, T., Tokuda, K., et al. 2020, ApJL, 904, L24, doi: 10.3847/2041-8213/abc884

Sato, F., & Fukui, Y. 1978, AJ, 83, 1607, doi: 10.1086/112370

Slane, P., Gaensler, B. M., Dame, T. M., et al. 1999, ApJ, 525, 357, doi: 10.1086/307893

Tachihara, K., Fukui, Y., Hayakawa, T., & Inoue, T. 2018, arXiv e-prints, arXiv:1811.02224. https://arxiv.org/abs/1811.02224

Tanaka, T., Uchida, H., Sano, H., & Tsuru, T. G. 2020, ApJL, 900, L5, doi: 10.3847/2041-8213/abaef0

Tanaka, T., Uchiyama, Y., Aharonian, F. A., et al. 2008, ApJ, 685, 988, doi: 10.1086/591020

Tsuji, N., Uchiyama, Y., Aharonian, F., et al. 2019, ApJ, 877, 96, doi: 10.3847/1538-4357/ab1b29

Zirakashvili, V. N., & Aharonian, F. A. 2010, ApJ, 708, 965, doi: 10.1088/0004-637X/708/2/965